INTERNATIONAL JOURNAL FOR NUMERICAL METHODS IN FLUIDS, VOL. 15, 1149–1170 (1992)

EFFECT OF RIVER DISCHARGE ON THE CIRCULATION IN THE WESTERN BAY OF BENGAL

S. K. DUBE, P. C. SINHA, G. S. RAO* AND A. D. RAO

Centre for Atmospheric Sciences, Indian Institute of Technology, New Delhi, 110 016, India

SUMMARY

A three-dimensional numerical model has been applied to study the impact of freshwater discharge from a river on the coastal circulation in the western Bay of Bengal. The basic dynamical framework of the model follows closely that described by Johns *et al.*[1] for the simulation of coastal upwelling off the east coast of India. Using this model, experiments have been performed to investigate the impact of the freshwater discharge at the location of Godavari river along the east coast of India. A comparison of the model results, with and without the inclusion of river discharge, shows that the river discharge into the western Bay of Bengal suppresses the upwelling near the river mouth. Though there are no detailed observations on the flow structure near the mouth of the Godavari river, the computed results are in qualitative agreement with the observations documented by Rao and Jayaraman[2] and Rao,[3] who have shown that during monsoon period the upwelling off Godavari estuary is suppressed.

KEY WORDS Coastal upwelling Turbulence energy Exchange coefficient Roughness length Co-ordinate transformation

INTRODUCTION

The hydrography of waters over the continental shelf and adjoining areas of the Bay of Bengal shows marked seasonal changes. This is in response to changing wind system and the freshwater discharge into the coastal area through the river systems. These freshwater discharges influence the characteristics of the coastal water.[3,4]

Associated with the monsoon system, the Indian subcontinent and the neighbouring areas receive considerable amount of precipitation. The precipitated water is discharged into the Bay of Bengal and the Arabian Sea at different locations. An examination of annual discharge of the major rivers indicates that the Bay of Bengal receives most of the river discharge (1283 km^3 per annum) and consequently the characteristics of the coastal waters are greatly influenced by it.

Johns *et al.*[1] have described a numerical model for the simulation of wind-induced coastal circulation in the western Bay of Bengal. The coastal boundary in the model was taken to be a vertical side-wall through which there is no flux of water. In actuality, however, there are a number of inlets joining the Bay of Bengal through which large quantity of fresh water is discharged into the sea during the monsoon season. Since this model does not take into account the effect of the water discharge from the rivers, it may lead to a misrepresentation of the circulation in the Bay of Bengal, particularly that near the coast during the monsoon season.

* Present affiliation: Kandla Port Trust, Gujarat, India.

0271–2091/92/221149–22$16.00

Received November 1991
Revised April 1992

Recognizing the above facts, in the present work, the numerical model described by Johns *et al.*[1] has been suitably modified by putting an open boundary at the location of the Godavari River (on the east coast of India). The location of the river is shown in Figure 1. Using this model, numerical experiments have been performed to investigate the impact of the river discharge on the circulation in the western Bay of Bengal. A comparison of the model results, with and without the inclusion of river discharge into the western Bay of Bengal, shows that the upwelling is suppressed in the former case. The computed results are in agreement with the observational studies of Rao and Jayaraman[2] and Rao.[3]

FORMULATION OF THE MODEL

For the formulation of the model, the analysis area, co-ordinate system and the governing equations are analogous to that described by Johns *et al.*[1] All conditions are referred to a local system of rectangular Cartesian co-ordinates $Oxyz$ with the origin, O, located in the equilibrium level of the sea surface. A coastal boundary, representing part of the east coast of India, is situated at $x=b_1(y)$ and an open-sea boundary corresponds to $x=b_2(y)$. Alongshore boundaries are situated, respectively, at $y=0$ and $y=L$.

The displaced position of the sea surface is given by $z=\zeta(x, y, t)$ and the position of the sea floor corresponds to $z=-h(x, y)$. Reynolds-averaged components of velocity u, v and w then satisfy

$$\frac{\partial u}{\partial t}+u\frac{\partial u}{\partial x}+v\frac{\partial u}{\partial y}+w\frac{\partial u}{\partial z}-fv=-\frac{g}{\rho_0}\int_z^\zeta \frac{\partial \rho}{\partial x}\,dz-g\frac{\partial \zeta}{\partial x}+\frac{1}{\rho_0}\frac{\partial \tau_x}{\partial z} \tag{1}$$

$$\frac{\partial v}{\partial t}+u\frac{\partial v}{\partial x}+v\frac{\partial v}{\partial y}+w\frac{\partial v}{\partial z}+fu=-\frac{g}{\rho_0}\int_z^\zeta \frac{\partial \rho}{\partial y}\,dz-g\frac{\partial \zeta}{\partial y}+\frac{1}{\rho_0}\frac{\partial \tau_y}{\partial z} \tag{2}$$

In (1) and (2), f denotes the Coriolis parameter, ρ the local density of the water and ρ_0 is a reference density. τ_x and τ_y denote components of Reynolds stress.

In this paper the density, ρ, is determined solely by the temperature of the water and we apply an equation of state in which

$$\rho=\rho_0[1-\alpha(T-T_0)] \tag{3}$$

In (3), T denotes the temperature of the water, α is a thermal expansion coefficient taken as 0·0002/°C and T_0 is the temperature corresponding to the density ρ_0. The dynamical boundary condition along the coastline is simply

$$u-vb_1'(y)=0 \quad \text{at } x=b_1(y), \tag{4}$$

where the prime denotes a differentiation with respect to y. This condition is used when no input of river discharge is considered.

When the input of river discharge is taken into account, the boundary condition (4) gets modified to

$$u-v\frac{\partial b_1}{\partial y}=\frac{Q}{BH}=bU. \tag{5}$$

Here Q denotes the volume of the river discharge into the western Bay of Bengal, per unit time and B is the breadth of the river. Appropriate boundary conditions at the open-sea boundaries are problematical and in this paper we apply radiation conditions identical to those used by

Johns *et al.*[1] These have the form

$$\bar{u}-\bar{v}b_2'(y)-(g/h)^{1/2}\zeta=0 \quad \text{at } x=b_2(y), \tag{6}$$

$$\bar{v}+(g/h)^{1/2}\zeta=0 \quad \text{at } y=0, \tag{7}$$

$$\bar{v}-(g/h)^{1/2}\zeta=0 \quad \text{at } y=L. \tag{8}$$

Here, $\bar{u}$ and $\bar{v}$ denote the depth-averaged components of current defined by

$$(\bar{u}, \bar{v})=\frac{1}{H}\int_{-h}^{\zeta}(u, v)\,dz, \tag{9}$$

where H is the total depth, $\zeta+h$. In (6) an approximation has been made involving the neglect of a small term $[b_2'(y)]^2$.

No-slip condition is applied at the impermeable sea floor:

$$u=v=w=0 \quad \text{at } z=-h. \tag{10}$$

At the sea surface, the internal Reynolds stress, (τ_x, τ_y), must equal the applied surface wind stress $(\tau_x^\zeta, \tau_y^\zeta)$ and, so,

$$\tau_x=\tau_x^\zeta, \qquad \tau_y=\tau_y^\zeta \quad \text{at } z=\zeta. \tag{11}$$

The surface kinematical condition requires that

$$\frac{\partial\zeta}{\partial t}+u\frac{\partial\zeta}{\partial x}+v\frac{\partial\zeta}{\partial y}-w=0 \quad \text{at } z=\zeta. \tag{12}$$

The equation of continuity leads to a diagnostic form for w in which

$$w=-\int_{-h}^{z}\left(\frac{\partial u}{\partial x}+\frac{\partial v}{\partial y}\right)dz \tag{13}$$

and, in vertically integrated form, may be written

$$\frac{\partial\zeta}{\partial t}+\frac{\partial}{\partial x}(H\bar{u})+\frac{\partial}{\partial y}(H\bar{v})=0. \tag{14}$$

Turbulence closure in the dynamical equation is achieved by making a gradient transfer hypothesis in which

$$\tau_x=K_M\rho_0\frac{\partial u}{\partial z}, \qquad \tau_y=K_M\rho_0\frac{\partial v}{\partial z}, \tag{15}$$

where the exchange coefficient, K_M, is subsequently related to the turbulence energy. The temperature, T, satisfies an advection–diffusion equation of the form

$$\frac{\partial T}{\partial t}+u\frac{\partial T}{\partial x}+v\frac{\partial T}{\partial y}+w\frac{\partial T}{\partial z}=\frac{\partial}{\partial z}\left(K_T\frac{\partial T}{\partial z}\right). \tag{16}$$

Boundary conditions to accompany (16) are

$$\frac{\partial T}{\partial z}=0 \quad \text{at } z=-h \text{ and } z=\zeta. \tag{17}$$

The coastal boundary is taken to be perfectly insulating, with no heat transfer between land and sea. During fluid outflow across the open-sea boundaries, the boundary temperature is

determined by thermal advection from the interior of the analysis area. During fluid inflow, the boundary temperature is prescribed and, in our application, is held fixed according to its specified initial value just outside of the open-sea boundaries. Such a prescription will be automatically included in our choice of the finite difference discretization of (16).

The value of the exchange coefficient is determined by an application of the equation for the turbulence energy density, E, in the system. This has the form

$$\frac{\partial E}{\partial t}+u\frac{\partial E}{\partial x}+v\frac{\partial E}{\partial y}+w\frac{\partial E}{\partial z}=K_M\left[\left(\frac{\partial u}{\partial z}\right)^2+\left(\frac{\partial v}{\partial z}\right)^2\right]+\frac{g}{\rho_0}K_T\frac{\partial \rho}{\partial z}+\frac{\partial}{\partial z}\left(K_E\frac{\partial E}{\partial z}\right)-\varepsilon. \tag{18}$$

In (18), K_E is an exchange coefficient for the vertical diffusive flux of turbulence energy. Other terms on the right-hand side represent, respectively: (i) shear production of turbulence energy; (ii) the suppressive effect on the production of turbulence of a stable vertical density stratification; (iii) the redistribution of turbulence energy by the turbulence itself; (iv) the dissipation of turbulence energy.

The boundary condition to accompany (18) states that there is no vertical exchange of turbulence energy across either the sea floor or the sea surface, thus leading to

$$\frac{\partial E}{\partial z}=0 \quad \text{at } z=-h \text{ and } z=\zeta. \tag{19}$$

Following Johns *et al.*,[1] the exchange coefficients are parameterized as

$$\begin{aligned} K_M &= c^{1/4} l E^{1/2}+N, \\ K_T &= K_E = c^{1/4} l E^{1/2}, \\ \xi &= c^{3/4} E^{3/2}/l. \end{aligned} \tag{20}$$

In (20), the constant, c, is set equal to 0·08 and N is an externally prescribed mixing coefficient whose characteristic mid-depth value is 10^{-2} m^2 s^{-1} and which reduces to negligible values both near the sea surface and the sea floor.

The length scale, l, is chosen as[1]

$$l=\frac{\kappa}{1/(z+h+z_{ob})+1/(\zeta-z+z_{os})} \tag{21}$$

where z_{ob} and z_{os} are, respectively, bottom and surface roughness lengths and κ is von Karman's constant. In our application, we take $z_{ob}=z_{os}=0{\cdot}1$ cm.

Using (3) and (15), equations (1) and (2) may be written as

$$\frac{\partial u}{\partial t}+u\frac{\partial u}{\partial x}+v\frac{\partial u}{\partial y}+\omega\frac{\partial u}{\partial z}-fv=-g\frac{\partial \zeta}{\partial x}+g\alpha\int_z^\zeta \frac{\partial T}{\partial x}\mathrm{d}z+\frac{\partial}{\partial z}\left(K_M\frac{\partial u}{\partial t}\right), \tag{22}$$

$$\frac{\partial v}{\partial t}+u\frac{\partial v}{\partial x}+v\frac{\partial v}{\partial y}+\omega\frac{\partial v}{\partial z}+fu=-g\frac{\partial \zeta}{\partial y}+g\alpha\int_z^\zeta \frac{\partial T}{\partial x}\mathrm{d}z+\frac{\partial}{\partial z}\left(K_M\frac{\partial v}{\partial t}\right). \tag{23}$$

CO-ORDINATE TRANSFORMATION

A system of transformed co-ordinates described by Johns *et al.*,[5] which facilitates the incorporation of irregular coastal and bottom topography has been used. This involves the introduction of

a new variable, ξ, determined by

$$\xi=[x-b_1(y)]/b(y), \tag{24}$$

where $b(y)=b_2(y)-b_1(y)$.

The vertical co-ordinate is similarly transformed to facilitate the implementation of boundary conditions at the sea-floor and the sea-surface. This leads to a new variable, σ, defined by

$$\sigma=\frac{z+h}{H}. \tag{25}$$

With ξ, y, σ and t as new independent variables and using (14) and (16), equations (1) and (2) may be readily transformed into

$$\frac{\partial u}{\partial t}+U\frac{\partial u}{\partial \xi}+v\frac{\partial u}{\partial y}+\omega\frac{\partial u}{\partial \sigma}-fv=-\frac{g}{b(y)}\frac{\partial \zeta}{\partial \xi}+\frac{g\alpha}{b(y)}\left[\int_0^1\frac{\partial}{\partial \xi}(HT)\,\mathrm{d}\sigma-\frac{\partial \zeta}{\partial \xi}T_{\sigma=1}+\left(\frac{\partial h}{\partial \xi}-\sigma\frac{\partial H}{\partial \xi}\right)T\right]$$
$$+\frac{1}{H^2}\frac{\partial}{\partial \sigma}\left(K_M\frac{\partial u}{\partial \sigma}\right), \tag{26}$$

$$\frac{\partial v}{\partial t}+U\frac{\partial v}{\partial \xi}+v\frac{\partial v}{\partial y}+\omega\frac{\partial v}{\partial \sigma}+fu=-g\frac{\partial \zeta}{\partial y}+\frac{g}{b(y)}[b_1'(y)+\xi b'(y)]\frac{\partial \zeta}{\partial \xi}$$
$$+g\alpha\left[\int_0^1\frac{\partial}{\partial y}(HT)\,\mathrm{d}\sigma-\frac{\partial \zeta}{\partial y}T_{\sigma=1}+\left(\frac{\partial h}{\partial y}-\sigma\frac{\partial H}{\partial y}\right)T\right]$$
$$-\frac{g\alpha}{b(y)}\left[b_1'(y)+\xi b'(y)\right]\left[\int_0^1\frac{\partial}{\partial \xi}(HT)\,\mathrm{d}\sigma-\frac{\partial \zeta}{\partial \xi}T_{\sigma=1}-\left(\frac{\partial h}{\partial \xi}-\frac{\partial H}{\partial \xi}\right)T\right]$$
$$+\frac{1}{H^2}\frac{\partial}{\partial \sigma}\left(K_M\frac{\partial v}{\partial \sigma}\right). \tag{27}$$

In (24) and (25),

$$U=[u-(b_1'+\xi b')v]/b \tag{28}$$

and

$$\omega=\sigma_t+u\sigma_x+v\sigma_y+w\sigma_z, \tag{29}$$

where the primes and subscripts refer to differentiations.

Equation (14) leads to

$$\frac{\partial}{\partial t}(b\zeta)+\frac{\partial}{\partial \xi}(bH\bar{U})+\frac{\partial}{\partial y}(bH\bar{v})=0, \tag{30}$$

where $\bar{U}$ denotes the depth-averaged value of U.

Following Johns,[6] ω is readily found to satisfy the diagnostic equation

$$\frac{\partial}{\partial \xi}[bH(U-\bar{U})]+\frac{\partial}{\partial y}[bH(v-\bar{v})]+\frac{\partial}{\partial \sigma}(bH\omega)=0. \tag{31}$$

In a similar manner, the temperature equation (16) may be transformed to yield

$$\frac{\partial T}{\partial t}+U\frac{\partial T}{\partial \xi}+v\frac{\partial T}{\partial y}+\omega\frac{\partial T}{\partial \sigma}=\frac{1}{H^2}\frac{\partial}{\partial \sigma}\left(K_T\frac{\partial T}{\partial \sigma}\right). \tag{32}$$

The energy equation (18) may be readily transformed into

$$\frac{\partial E}{\partial t}+U\frac{\partial E}{\partial \xi}+v\frac{\partial E}{\partial y}+\omega\frac{\partial E}{\partial \sigma}=\frac{K_M}{H^2}\left[\left(\frac{\partial u}{\partial \sigma}\right)^2+\left(\frac{\partial v}{\partial \sigma}\right)^2\right]+\frac{1}{H^2}\frac{\partial}{\partial \sigma}\left(K_E\frac{\partial E}{\partial \sigma}\right)-\varepsilon-\frac{g\alpha}{H}K_T\frac{\partial T}{\partial \sigma}. \quad (33)$$

The advantage of this co-ordinate transformation is that the lateral sea-floor and sea-surface boundary conditions are expressible in a form ideally suited to the subsequent numerical treatment. Specially, (4) and (6) are satisfied provided that

$$U=0 \quad \text{at } \xi=0 \quad (34)$$

and

$$b(y)\bar{U}-(g/h)^{1/2}\zeta=0 \quad \text{at } \xi=1. \quad (35)$$

The sea-surface conditions (11) and (12), when combined with (15), lead to

$$K_M\frac{\partial u}{\partial \sigma}=H\tau_x^{\zeta}/\rho, \qquad K_M\frac{\partial v}{\partial \sigma}=H\tau_y^{\zeta}/\rho \quad \text{at } \sigma=1. \quad (36)$$

The kinematic condition (12) is equivalent to

$$\omega=0 \quad \text{at } \sigma=1, \quad (37)$$

whilst the temperature condition (17) is satisfied provided that

$$\frac{\partial T}{\partial \sigma}=0 \quad \text{at } \sigma=0 \text{ and } \sigma=1. \quad (38)$$

The energy condition (19) transforms to

$$\frac{\partial E}{\partial \sigma}=0 \quad \text{at } \sigma=0 \text{ are } \sigma=1. \quad (39)$$

The sea-floor conditions (10) are equivalent to

$$u=v=\omega=0 \quad \text{at } \sigma=0 \quad (40)$$

In terms of this 'σ-co-ordinate' formulation, (9) yields the depth-averaged current in the form

$$(\bar{u},\bar{v})=\int_0^1 (u,v)\,d\sigma. \quad (41)$$

It would now be straightforward to develop a finite difference analogue of this system of transformed equations in which there is a uniform spacing of computational grid points in the ξ-direction. However, a prominent feature of upwelling is its effective confinement to within a distance from the coastline having the order of the baroclinic radius of deformation. A uniform spacing in ξ would, therefore, necessitate an overall cross-shelf resolution in excess of that allowed by the computer resources. Similar remarks apply to the discretization of the σ-variable, where a high resolution of the dynamics is required near both $\sigma=0$ and $\sigma=1$. It is, therefore, expedient to introduce a further transformation of the horizontal as well as the vertical co-ordinates to achieve this end. Accordingly, the horizontal ξ-co-ordinate is transformed as

$$\chi=\xi+\lambda\ln\left(\frac{\xi+\xi_0}{\xi_0}\right), \quad (42)$$

where λ and ξ_0 ($\ll 1$) are disposable parameters. With an appropriate choice of these, and with a discretization of the χ-variable in which there is a uniform spacing between grid points, there is a substantial mesh refinement near $\xi = 0$. In this region, the grid spacing is reduced to a fraction of its essentially uniform value between $\xi = 0{\cdot}5$ and $\xi = 1{\cdot}0$.

Following Johns *et al.*,[5] a transformation of the $\sigma-$variable is introduced according to

$$\sigma + \sigma_0 = \sigma_0 \exp \psi(\eta), \tag{43}$$

where σ_0 ($\ll 1$) is a disposable parameter,

$$\psi(\eta) = \eta - \frac{1}{2\eta_s}(1-\sigma_0)\eta^2 \tag{44}$$

and

$$\eta_s = \frac{2\ln(1+1/\sigma_0)}{(1+\sigma_0)}. \tag{45}$$

From (42)–(44) it is readily seen that finite difference increments $\Delta\sigma$ and $\Delta\eta$ are related by

$$\Delta\sigma = \sigma_0\left[1 - \frac{1}{\eta_s}(1-\sigma_0)\eta\right]\exp\psi(\eta)\,\Delta\eta. \tag{46}$$

On discretizing the η-variable using a constant grid spacing, this leads to increased resolution near both $\sigma = 0$ and $\sigma = 1$ compared to that in the mid-depths.

In terms of the final transformed variables, the coastal boundary and the off-shore open-sea boundary correspond, respectively, to $\chi = 0$ and $\chi = \chi_m = 1 + \lambda \ln[1 + (1/\xi_0)]$. The sea floor and sea surface correspond, respectively, to $\eta = 0$ and $\eta = \eta_s = 2\ln(1+1/\sigma_0)/(1+\sigma_0)$.

Then, by writing

$$\left.\begin{aligned} \frac{\partial\xi}{\partial\chi} &= F(\chi) = \frac{1}{1+\lambda/(\xi+\xi_0)} \\ \text{and} \qquad \beta(\eta) &= \frac{\partial\sigma}{\partial\eta}. \end{aligned}\right\} \tag{47}$$

In the new co-ordinates (χ, y, η, t), equations (30)–(31), (26)–(27) and (32)–(33) are further transformed to

$$\frac{\partial}{\partial t}(b\zeta) + \frac{1}{F}\frac{\partial}{\partial\chi}(bH\bar{U}) + \frac{\partial}{\partial y}(bH\bar{v}) = 0, \tag{48}$$

$$\frac{1}{F}\frac{\partial}{\partial\chi}[bH(U-\bar{U})] + \frac{\partial}{\partial y}[(v-\bar{v})] + \frac{1}{\beta}\frac{\partial}{\partial\eta}(bH\omega) = 0, \tag{49}$$

$$\begin{aligned} \frac{\partial\tilde{u}}{\partial t} + \frac{1}{F}\frac{\partial}{\partial\chi}(U\tilde{u}) + \frac{\partial}{\partial y}(v\tilde{u}) + \frac{1}{\beta}\frac{\partial}{\partial\eta}(\omega\tilde{u}) - f\tilde{v} = &-\frac{gH}{F}\frac{\partial\xi}{\partial\chi} + \frac{g\alpha H}{F}\left[\int_0^{\eta_s}\frac{\partial}{\partial\chi}(\beta HT)\,d\eta - \frac{\partial\zeta}{\partial\chi}T_{\sigma=1}\right. \\ &\left. + \left(\frac{\partial h}{\partial\chi} - \sigma\frac{\partial H}{\partial\chi}\right)T\right] + \frac{1}{H^2\beta}\frac{\partial}{\partial\eta}\left(\frac{K_M}{\beta}\frac{\partial\tilde{u}}{\partial\eta}\right), \end{aligned} \tag{50}$$

$$\frac{\partial \tilde{v}}{\partial t}+\frac{1}{F}\frac{\partial}{\partial \chi}(U\tilde{v})+\frac{\partial}{\partial y}(v\tilde{v})+\frac{1}{\beta}\frac{\partial}{\partial \eta}(\omega\tilde{v})+f\tilde{u}$$
$$=-gH\left[b\frac{\partial \zeta}{\partial y}-\left(\frac{b'_1+\xi b'}{F}\right)\frac{\partial \zeta}{\partial \chi}+g\alpha bH\left[\int_0^{\eta_s}\frac{\partial}{\partial y}(\beta HT)\,d\eta-\frac{\partial \zeta}{\partial y}T_{\sigma=1}+\left(\frac{\partial h}{\partial y}-\sigma\frac{\partial H}{\partial y}\right)T\right]\right.$$
$$\left.-\frac{g\alpha H}{F}(b'_1+\xi b')\left[\int_0^{\eta_s}\frac{\partial}{\partial \chi}(\beta HT)\,d\eta-\frac{\partial \zeta}{\partial \chi}T_{\sigma=1}-\left(\frac{\partial h}{\partial \chi}-\sigma\frac{\partial H}{\partial \chi}\right)T\right]+\frac{1}{H^2\beta}\frac{\partial}{\partial \eta}\left(\frac{K_M}{\beta}\frac{\partial \tilde{v}}{\partial \eta}\right),\right. \tag{51}$$

$$\frac{\partial \tilde{T}}{\partial t}+\frac{1}{F}\frac{\partial}{\partial \chi}(U\tilde{T})+\frac{\partial}{\partial y}(v\tilde{T})+\frac{1}{\beta}\frac{\partial}{\partial \eta}(\omega\tilde{T})=\frac{1}{H^2\beta}\left(\frac{K_M}{\beta}\frac{\partial \tilde{T}}{\partial \eta}\right), \tag{52}$$

$$\frac{\partial \tilde{E}}{\partial t}+\frac{1}{F}\frac{\partial}{\partial \chi}(U\tilde{E})+\frac{\partial}{\partial y}(v\tilde{E})+\frac{1}{\beta}\frac{\partial}{\partial \eta}(\omega\tilde{E})=\frac{K_M}{H^3\beta^2 b}\left[\left(\frac{\partial \tilde{u}}{\partial \eta}\right)^2+\left(\frac{\partial \tilde{v}}{\partial \eta}\right)^2\right]+\frac{1}{H^2\beta}\frac{\partial}{\partial \eta}\left(\frac{K_E}{\beta}\frac{\partial \tilde{E}}{\partial \eta}\right)$$
$$-bH\varepsilon-\frac{g\alpha K_T}{H\beta}\left(\frac{\partial \tilde{T}}{\partial \eta}\right). \tag{53}$$

Equations (41) and (44) show that the depth-averaged velocity is determined from

$$(\bar{u},\bar{v})=\int_0^{\eta_s}(u,v)\beta(\eta)\,d\eta, \tag{54}$$

where the new prognostic variables are defined by

$$\tilde{u},\tilde{v},\tilde{T},\tilde{E}=bH(u,v,T,E).$$

The applied surface wind conditions (36) lead to

$$\frac{K_M}{\beta}\frac{\partial \tilde{u}}{\partial \eta}=bH^2\tau_x^{\zeta}/\rho_0,\qquad \frac{K_M}{\beta}\frac{\partial \tilde{v}}{\partial \eta}=bH^2\tau_y^{\zeta}/\rho_0\quad\text{at }\eta=\eta_s, \tag{55}$$

whilst, in the 'η-co-ordinate' formulation, the other sea-floor and sea-surface conditions have obvious forms. Equations (48)–(53), together with their corresponding boundary conditions, form the final version of the equations used in the numerical model.

NUMERICAL PROCEDURE

The final transformed equations (48)–(53) form the basis for a set of finite difference analogues. The co-ordinates (χ, y, η, t) are discretized as follows:

$$\begin{aligned}
&\chi=\chi_i=(i-1)\Delta\chi, && i=1(1)m; \quad \Delta\chi=\chi_m/(m-1),\\
&y=y_j=(j-1)\Delta y, && j=1(1)n; \quad \Delta y=L/(n-1),\\
&\eta=\eta_k=(k-1)\Delta\eta, && k=1(1)q; \quad \Delta\eta=\eta_q/(q-1),\\
&t=t_p=p\Delta t, && p=0,1,2,\ldots.
\end{aligned} \tag{56}$$

In this prescription m and n are, respectively, even and odd integers.

A horizontal staggered grid is used in which there are three distinct types of points. When i is even and j is odd, the point is a ζ-point at which both ζ and T are computed. If i is odd and j is odd, the point is a u-point at which u, U and E are computed. If i is even and j is even, the point is a v-point at which v is computed. The coastline, therefore, consists of u- and U-points. The off-shore open-sea boundary consists of ζ-points and v-points and the alongshore open-sea

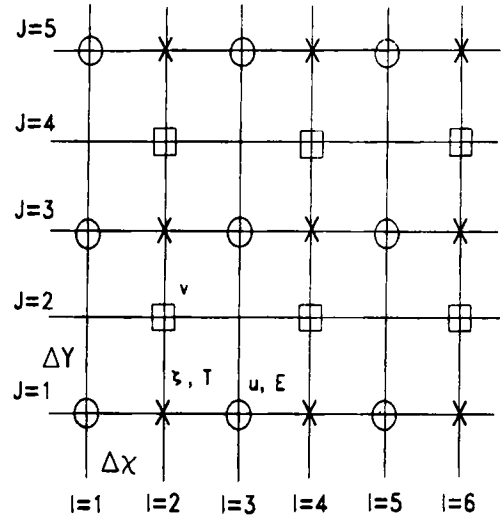

(a)

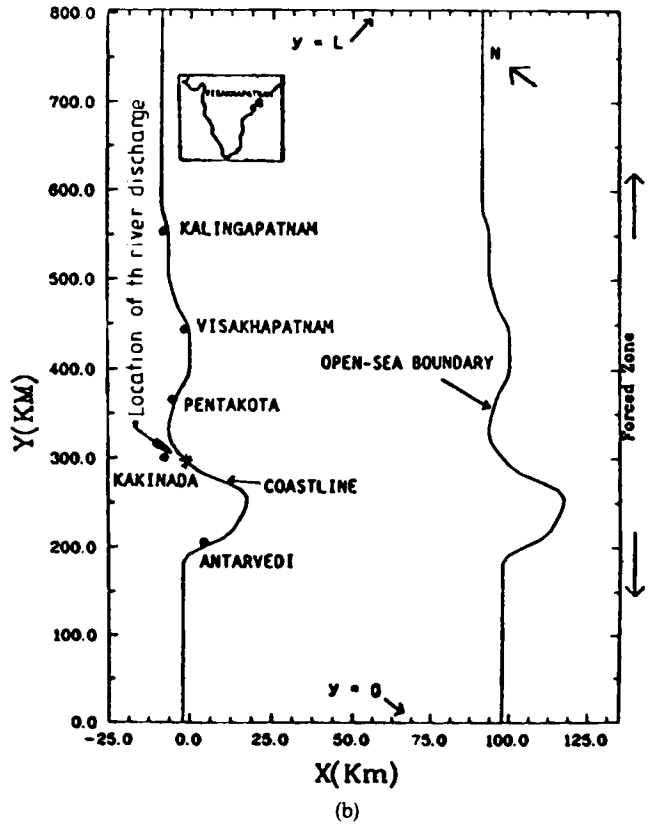

(b)

Figure 1. (a) Analysis region. (b) Computational grid arrangement

boundaries consist of ζ-points and u-points. A suitable arrangement of grid points in the (χ, y) plane is shown in Figure 1(a).

The finite difference discretization of the horizontal co-ordinates has been described in detail in Johns *et al.*[3] and hence not repeated here. It is, however, appropriate to describe the essentials of the discretization process as applied to the vertical co-ordinate, η. The most important features of this relate to the treatment of the diffusion terms.

As for the vertical co-ordinate and the time variable, we have

$$\eta=\eta_k=(k-1)\,\Delta\eta, \quad k=1, 2, \ldots, q \quad \Delta\eta=\eta_s/(q-1), \tag{57}$$
$$t=t_p=p\,\Delta t, \quad p=0, 1, \ldots$$

and, for any variable X,

$$X(\chi, y, \eta_k, t_p)=X_k^p. \tag{58}$$

Vertical differencing and averaging operations are defined by

$$\delta_\eta X=(X_{k+1/2}^p-X_{k-1/2}^p)/\Delta\eta, \tag{59}$$
$$\bar{X}^\eta=\tfrac{1}{2}(X_{k+1/2}^p+K_{k-1/2}^p) \tag{60}$$

and a shift operator by

$$E_t(X)=X_k^{p+1}. \tag{61}$$

The following typical discretizations are then used:

$$\frac{\partial}{\partial\eta}\left(\frac{K_M}{\beta}\frac{\partial\tilde{u}}{\partial\eta}\right)=\delta_\eta\left[\left(\frac{K_M}{\beta}\right)^{-\eta}\delta_\eta(E_t\tilde{u})\right] \tag{62}$$

and

$$\varepsilon=\frac{c^{3/4}\,\tilde{E}^{1/2}\,E_t(\tilde{E})}{H^{3/2}\,b^{3/2}\,l}. \tag{63}$$

The semi-implicit nature of the (62) and (63) guarantees unconditional computational stability with reference to the diffusion and dissipative terms in (50)–(53). A further important feature of (62) is its conservation characteristic and the fact that the wind stress conditions (55) must be applied at $\eta=(q-1/2)\,\Delta\eta$. The latter fact is an additional reason why the vertical grid spacing near the sea surface should ideally be as fine as possible.

It will be noted that the implementation of the numerical scheme based upon (62) requires the application of three Gaussian elimination procedures as the solution is advanced through each time step Δt. However, in comparison with an explicit treatment, this is a small price to pay, bearing in mind the reduction in Δt that would be necessary with the subsequent ultrafine grid spacing near $\sigma=0$.

The discretization scheme used for (52) is of central importance in the solution procedure. It is based upon an upstream scheme described by Roache[7] and on satisfying the transportive condition. This means that a necessarily positive-definite physical quantity may be advected through the system without any spurious change of sign that might result from the application of

a centred scheme. Equation (52) is discretized as

$$\frac{\tilde{T}^{p+1}_{i,j,k}-\tilde{T}^{p}_{i,j,k}}{\Delta t}+\frac{1}{F_i}\frac{1}{4\Delta\chi}[(U^{p}_{i+1,j,k}-|U^{p}_{i+1,j,k}|)\tilde{T}^{p}_{i+2,j,k}$$
$$+(U^{p}_{i+1,j,k}+|U^{p}_{i+1,j,k}|-U^{p}_{i-1,j,k}+|U^{p}_{i-1,j,k}|)\tilde{T}^{p}_{i,j,k}$$
$$-(U^{p}_{i-1,j,k}+|U^{p}_{i-1,j,k}|)\tilde{T}^{p}_{i-2,j,k}]+\frac{1}{4\Delta y}[(v^{p}_{i,j+1,k}-|v^{p}_{i,j+1,k}|)\tilde{T}^{p}_{i,j+2,k}+(v^{p}_{i,j+1,k}+|v^{p}_{i,j+1,k}|$$
$$-v^{p}_{i,j-1,k}+|v^{p}_{i,j-1,k}|)\tilde{T}^{p}_{i,j,k}-(v^{p}_{i,j-1,k}+|v^{p}_{i,j-1,k}|)\tilde{T}^{p}_{i,j-2,k}]$$
$$+\frac{1}{4\beta_k}\frac{1}{\Delta\eta}[(\omega^{p}_{i,j,k+1}+\omega^{p}_{i,j,k})(\tilde{T}^{p}_{i,j,k+1}+\tilde{T}^{p}_{i,j,k})$$
$$-(\omega^{p}_{i,j,k}+\omega^{p}_{i,j,k-1})(\tilde{T}^{p}_{i,j,k}+\tilde{T}^{p}_{i,j,k-1})]$$
$$=\frac{1}{(H^{p+1}_{i,j})^2\beta_k}\frac{1}{2(\Delta\eta)^2}\left\{\left[\left(\frac{K_T}{\beta}\right)^{p}_{i,j,k+1}+\left(\frac{K_T}{\beta}\right)^{p}_{i,j,k}\right]\tilde{T}^{p+1}_{i,j,k+1}\right.$$
$$+\left[\left(\frac{K_T}{\beta}\right)^{p}_{i,j,k}+\left(\frac{K_T}{\beta}\right)^{p}_{i,j,k-1}\right]\tilde{T}^{p+1}_{i,j,k-1}-\left[\left(\frac{K_T}{\beta}\right)^{p}_{i,j,k+1}\right.$$
$$\left.\left.+2\left(\frac{K_T}{\beta}\right)^{p}_{i,j,k}+\left(\frac{K_T}{\beta}\right)^{p}_{i,j,k-1}\right]\tilde{T}^{p+1}_{i,j,k}\right\}. \tag{64}$$

Equation (64), together with the boundary conditions, is again solved by a Gaussian elimination method to obtain the values of $\tilde{T}$ at ζ-points.

In contrast to equations (50), (51) and (53), where the discretization of the horizontal advection terms are neglected at the open-sea boundaries ($i=m-1$, $j=2$ and $j=n-1$), the horizontal thermal advection terms are retained at the open-sea boundaries ($i=m$, $j=1$ and $j=n$) and at the mouth of the river ($i=1$ and $j=9$).

The horizontal thermal advection term at $i=m$ is discretized as

$$\frac{1}{F_m}\frac{1}{4\Delta\chi}[(U^{p}_{m+1,j,k}-|U^{p}_{m+1,j,k}|)\tilde{T}^{p}_{m+2,j,k}$$
$$+(U^{p}_{m+1,j,k}+|U^{p}_{m+1,j,k}|-U^{p}_{m-1,j,k}+|U^{p}_{m-1,j,k}|)\tilde{T}^{p}_{m,j,k}$$
$$-(U^{p}_{m-1,j,k}+|U^{p}_{m-1,j,k}|)\tilde{T}^{p}_{m-2,j,k}]. \tag{66}$$

It may be seen that this discretization references the values of U and T outside the analysis area. To overcome this difficulty, $U^{p}_{m+1,j,k}$ is replaced by $U^{p}_{m-1,j,k}$ and $\tilde{T}^{p}_{m+2,j,k}$ is prescribed initially ($=\tilde{T}_{\text{east}}$) and is held temporally invariant. With this assumption, the discretized form of (66) becomes

$$\frac{1}{F_m}\frac{1}{4\Delta\chi}[(U^{p}_{m-1,j,k}-|U^{p}_{m-1,j,k}|)\tilde{T}^{p}_{\text{east},j,k}+2|U^{p}_{m-1,j,k}|\tilde{T}^{p}_{m,j,k}-(U^{p}_{m-1,j,k}+|U^{p}_{m-1,j,k}|)\tilde{T}^{p}_{m-2,j,k}]. \tag{67}$$

During outflow of the fluid where $U^{p}_{m-1,j,k}$ is positive, the first term in the square bracket of (67) becomes zero. Thus, the horizontal thermal advection at the eastern open-sea boundary is calculated by reference to the value of the temperature at the boundary $i=m$ and at $i=m-2$.

During fluid inflow where $U^p_{m-1,j,k}$ is negative, the last term in the square bracket of (67) becomes zero and the horizontal thermal advection at the eastern open-sea boundary is calculated with reference to the value of the temperature at the boundary $i=m$ and the prescribed value at $i=m+2$.

The horizontal thermal advection term at $j=1$ is discretized as

$$\frac{1}{4\Delta y}[(v^p_{i,2,k}-|v^p_{i,2,k}|)\,\tilde{T}^p_{i,3,k}+(v^p_{i,2,k}+(|v^p_{i,2,k}|-v^p_{i,0,k}+|v^p_{i,0,k}|)\,\tilde{T}^p_{i,1,k}-(v^p_{i,0,k}+|v^p_{i,0,k}|)\,\tilde{T}^p_{i,-1,k}]. \tag{68}$$

From (68), it may be seen that the discretization references the values of v and T outside the analysis area. To avoid this difficulty, $v^p_{i,0,k}$ is replaced by $v^p_{i,2,k}$ and $\tilde{T}^p_{i,-1,k}$ is prescribed initially ($=T_{\text{south}}$) and is kept temporally invariant. With these assumptions, the discretized form of (68) becomes

$$\frac{1}{4\Delta y}[(v^p_{i,2,k}-|v^p_{i,2,k}|)\,\tilde{T}^p_{i,3,k}+2|v^p_{i,2,k}|\,\tilde{T}^p_{i,1,k}-(v^p_{i,2,k}+|v^p_{i,2,k}|)\,\tilde{T}^p_{i,\text{south},k}]. \tag{69}$$

During outflow of the fluid where $v^p_{i,2,k}$ is negative, the last term in the square bracket of (69) becomes zero and the horizontal thermal advection at the southern open-sea boundary is calculated by reference to the value of the temperature at the boundary $j=1$ and at $j=n$.

During fluid inflow where $v^p_{i,2,k}$ is positive, the first term in the square bracket of (69) becomes zero and the horizontal thermal advection term at the southern open-sea boundary is computed by reference to the value of the temperature at the boundary $j=1$ and the prescribed value outside the southern boundary.

The horizontal thermal advection term at $j=n$ is discretized as

$$\frac{1}{4\Delta y}[(v^p_{i,n+1,k}-|v^p_{i,n+1,k}|)\,\tilde{T}^p_{i,n+2,k}+(v^p_{i,n+1,k}+|v^p_{i,n+1,k}|-v^p_{i,n-1,}$$
$$+|v^p_{i,n-1,k}|)\,\tilde{T}^p_{i,n,k}-(v^p_{i,n-1,k}+|v^p_{i,n-1,k}|)\,\tilde{T}^p_{i,n-2,k}]. \tag{70}$$

It may be seen that (70) references the values of v and T outside the model domain. To overcome this difficulty, $v^p_{i,n+1,k}$ is replaced by $v^p_{i,n-1,k}$ and $\tilde{T}^p_{i,n+2,k}$ is prescribed initially ($=\tilde{T}_{\text{north}}$) and is held temporally invariant. With this assumption, the discretized form of (70) becomes

$$\frac{1}{4\Delta y}[(v^p_{i,n-1,k}-|v^p_{i,n-1,k}|)\,\tilde{T}^p_{i,\text{north},k}+2|v^p_{i,n-1,k}|\,\tilde{T}^p_{i,n,k}-(v^p_{i,n-1,k}+|v^p_{i,n-1,k}|)\,\tilde{T}^p_{i,n-2,k}]. \tag{71}$$

During outflow of the fluid where $v^p_{i,n-1,k}$ is positive, first term in the square bracket of (71) becomes zero. Thus, the horizontal thermal advection at the northern open-sea boundary is calculated by reference to the value of the temperature at the boundary $j=n$ and at $j=n-2$.

During fluid inflow where $v^p_{i,n-1,k}$ is negative, the last term in the square bracket of (71) becomes zero and the horizontal thermal advection term at the northern open-sea boundary is calculated by reference to the value of the temperature at the boundary $j=n$ and the prescribed value at $j=n+2$.

At the mouth of the river, i.e. for $i=1$ and $j=9$, an approach similar to that described above is used for discretization of thermal advection terms where temperature of the river water is prescribed and is kept invariant during integration.

During fluid outflow, the upstream property of the scheme means that the boundary temperature may be predicted. During fluid inflow, the same property of the scheme results in a reference being made to the flux of thermal energy into the analysis area. Thus, the use of an upstream scheme leads to a natural way of satisfying the boundary conditions on the thermal field at the open-sea boundaries. Owing to the conservative property of the scheme, any increase in the total thermal energy in the system is exactly balanced by a net inward flux of thermal energy across the open-sea boundaries.

In the analysis area as shown in Figure 1(b), Godavari River joins the Bay of Bengal at the location, which corresponds to $j=9$ of the grid arrangement. Along the coast, there are only u-points and, at each of these points, U is identically zero except at $j=9$, where the amount of the river discharge is prescribed.

It is essential to modify the boundary condition for the thermal energy equation (52) at $j=9$ of the western boundary of the analysis region ($\chi=0$). This is done in exactly the same manner as described in detail by Johns *et al.*[1] for open coastal boundaries.

NUMERICAL EXPERIMENTS

An analysis area is considered within which the origin, 0, is situated at 79·9°E, 15·2°N. The Oy axis is directed in a generally north-easterly direction and makes an angle of 53° with the north–south axis. This arrangement implies that the extent of the analysis region in the y-direction corresponds to $L=803$ km. The region is divided into three distinct sections. The most southerly of these, adjacent to $y=0$ and in which wind stress forcing is not applied, extends over a distance of approximately 146 km in the y-direction. Immediately to the north of this, a region of wind stress forcing extends to a distance of 444 km in the y-direction. To the north of this, there is again an unforced region bounded in the y-direction by $y=L$ and which has an extent of 213 km. The breadth of the analysis region (the distance from the coastline to open-sea boundary) is uniform and equal to 100 km. The coastline is modelled realistically between Antarvedi and Kalingapatnam, each of which lies within the forced region. To the south and north of these positions, the actual coastline topography is replaced by a hypothetical straight coastline pointing in the y-direction. This extends as far as $y=0$ and $y=L$. This general arrangement is shown in a plan view of the analysis region in Figure 1(b).

A smoothed bathymetry is derived by utilizing 98 spot depths from the relevant British Admiralty hydrographic chart and applying an interpolation based on distance-weighting to determine the local depth at any point in the analysis area.[8] Special attention has been given to the representation of the bathymetry in the forced region up to a distance of about 30 km from the coastline. Off-shore of this position, the depth is artificial and is almost constant near the off-shore open-sea boundary. This yields an optimum compatibility with the application of the radiation condition at the off-shore boundary.

The finite difference grid is fixed by taking $m=20$, $n=23$ and $q=36$. The values of ξ_0, λ, γ and σ_0 are set equal to 0·008, 0·04, 0·7 and 0·0001, respectively. This prescription implies that the off-shore grid increment near the coast is about 1·7 km and expands to about 6 km near the open-sea boundary. The implied grid increment in the y-direction is 36·5 km. In the deepest water, the implied near-bottom vertical grid increment is of order 1 m, whilst in the more shallow coastal upwelling zone, it is of order 0·2 m.

With this grid specification, it was found that computational stability could be maintained with a time step of 90 s and this value was used in all the experiments.

Experiments have been performed by an application of south-westerly wind stress in the forced zone [Figure 1(b)]. This wind stress is representative of the month of July. The magnitude of the

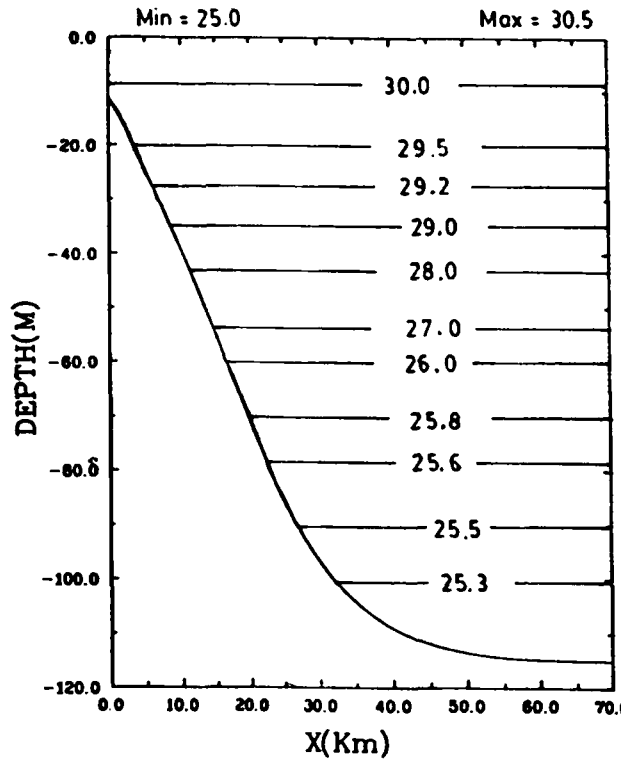

Figure 2. The initial field (°C) off $j=9$ (near Kakinada)

associated surface wind stress was determined in terms of the wind speed, V, and the surface density of air, ρ_a, by use of the bulk aerodynamic formula:

$$\tau=\rho_a C_D V|V|, \tag{72}$$

where the drag coefficient C_D is set equal to $1{\cdot}19\times10^{-3}$. This corresponds to a wind speed, V, equal to $6\,\mathrm{m\,s^{-1}}$ and ρ_a was taken as $1{\cdot}176\,\mathrm{kg\,m^{-3}}$.

Before the onset of wind stress forcing, the isotherms in the model are taken to be horizontal, with a stratification characteristic of that found in the Bay of Bengal in July.[9] For the cross-shelf section off $j=9$, the initial thermal field that is used in the experiments is shown in Figure 2.

In the present study numerical experiments have been performed, both with and without the inclusion of river discharge. The river discharge, Q, at $j=9$ is specified as $20\,000\,\mathrm{m^3\,s^{-1}}$. From an initial state of rest, the governing equations are integrated ahead in time for a period of six days, both with and without the prescribed river discharge.

RESULTS AND DISCUSSION

The computed thermal and dynamical fields, both with and without the inclusion of river discharge, are shown in Figures 3–12.

Figure 3 provides a comparison of the thermal field in a horizontal plane at day 2 in the region subject to south-westerly wind stress forcing, with and without the inclusion of river discharge. It

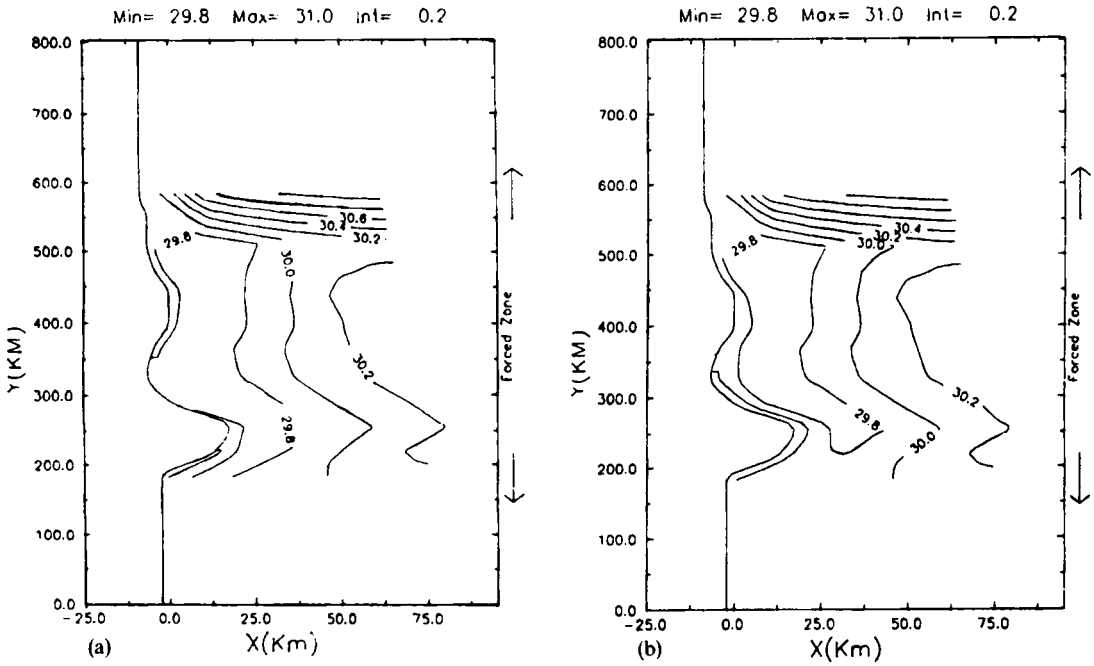

Figure 3. The computed thermal field (°C) in a horizontal plane at day 2: (a) without river discharge; (b) with river discharge

may be seen from Figure 3(a) that when there is no river discharge, the surface temperature near the coast is reduced to 29·8°C from its initial value of 30·5°C. This is the zone of coastal upwelling, which is confined to within a distance approximately equivalent to the baroclinic Rossby radius of deformation (about 20 km in the present application). An increase of surface temperature in the northern part of the forced zone is caused by the strong non-linear effect associated with the horizontal convergence, largely due to alongshore variations of the alongshore flow.

In the case when the river discharge is included [Figure 3(b)], the coastal upwelling is apparently suppressed, which is indicated by the replacement of the isotherm corresponding to the temperature 29·8°C by that of 30°C in the vicinity of the coast where the river joins the sea

Figure 4 gives a comparison of vertical thermal structure at day 2 in a transect off $j=9$ (near Kakinada), with and without the river discharge.

Figure 4(a) shows that when the river discharge is absent, a core of near-coastal surface water has formed with a temperature that has reduced to 30°C from its initial value of 30·5°C. In the case when the river discharge is taken into account [Figure 4(b)], the coastal upwelling is apparently suppressed as is indicated by the marked downwarping of the isotherm corresponding to the temperature of 30°C from its initial horizontal form. This may be attributed to the fact that the wind-induced off-shore transport of surface water is being compensated by the inflow of the river discharge. Hence, the continuity of mass is maintained near the coast and the subsurface water cannot rise upto the surface. This fact is consistent with the inferences of Rao and Jayaraman[2] and Rao[3] from the observational studies.

Figure 5 depicts a comparison of the surface circulation in a horizontal plane at day 2 in the region subject to south-westerly wind stress forcing, with and without the inclusion of river discharge. It may be seen from Figure 5(a) that when the river discharge is excluded, the surface

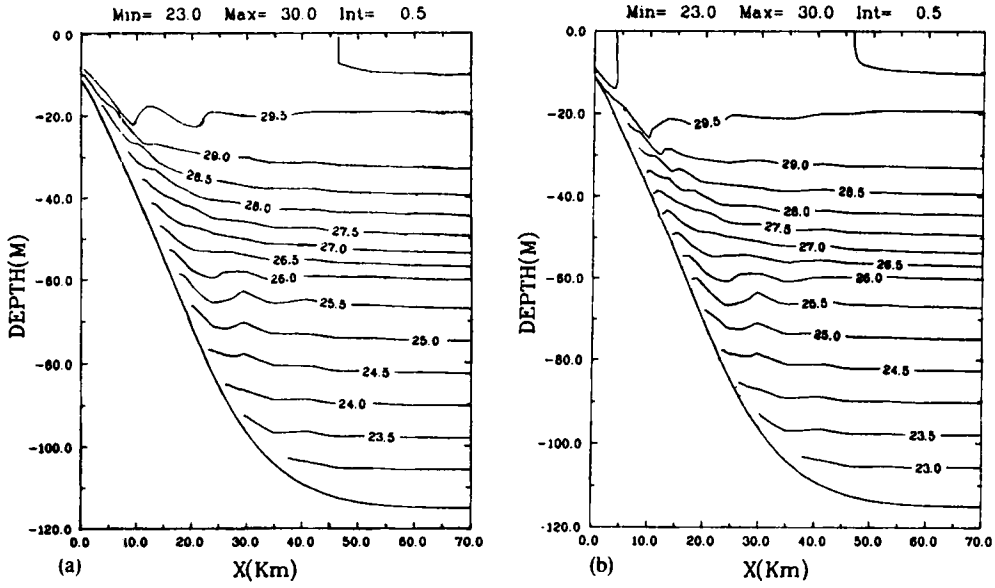

Figure 4. The computed thermal field (°C) off $j=9$ at day 2: (a) without river discharge; (b) with river discharge

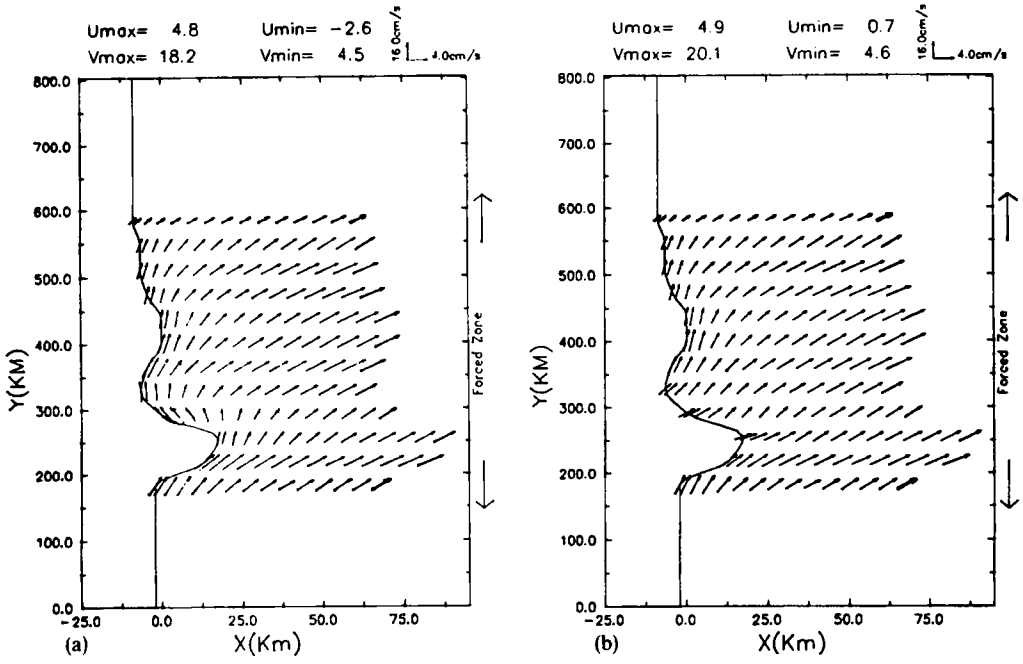

Figure 5. Plan view of the computed surface current vectors at day 2: (a) without river discharge; (b) with river discharge

currents, away from the constraining effect of the coastline, are aligned to flow essentially in the eastward direction. In the immediate vicinity of the coastline, the western boundary current is constrained to flow along the coast. Maximum computed off-shore cross-shelf velocities are about 5 cm s^{-1}, whilst on-shore velocities, induced locally by the curving coastline near Kakinada, attain a maximum of about 3 cm s^{-1}. Maximum and minimum computed alongshore velocities are, respectively, 18 and 4 cm s^{-1}. In the case when the river discharge is included [Figure 5(b)], the western boundary current weakens in the vicinity of the river and the surface currents are mainly directed eastwards. Maximum off-shore cross-shelf velocity is about 5 cm s^{-1}, whilst there is no on-shore velocity. Maximum and minimum longshore velocities are about 20 and 5 cm s^{-1}, respectively.

Figure 6 provides a comparison of the vertical current structure at day 2 in a transect off $j=9$, with and without considering the effect of river discharge. Figure 6(a) shows that when the river discharge is absent, an off-shore surface flow is apparent in this cross-section with a maximum speed of about 3 cm s^{-1}, with the exception of a strong on-shore surface flow with a maximum current velocity of 3·4 cm s^{-1} within about 15 km off the coastline. This on-shore surface flow is actually a part of the strong western boundary current flowing along the coast and has been discussed above [Figure 5(a)].

When the river discharge is taken into account [Figure 6(b)], the on-shore surface flow near the coast is replaced by an off-shore one leading to a maximum current velocity of about 3 cm s^{-1}. Figure 6(a) shows the existence of strong upwelling throughout the flow field, with a maximum upwelling velocity of about $4{\cdot}4 \times 10^{-3}$ cm s^{-1}, while in the case of Figure 6(b), the upwelling velocity has reduced to about $3{\cdot}6 \times 10^{-3}$ cm s^{-1}.

Figure 7 gives a comparison of the isolines of vertical longshore velocity structure at day 2 in a transect off $j=9$, with and without the inclusion of river discharge. It may be seen from Figure

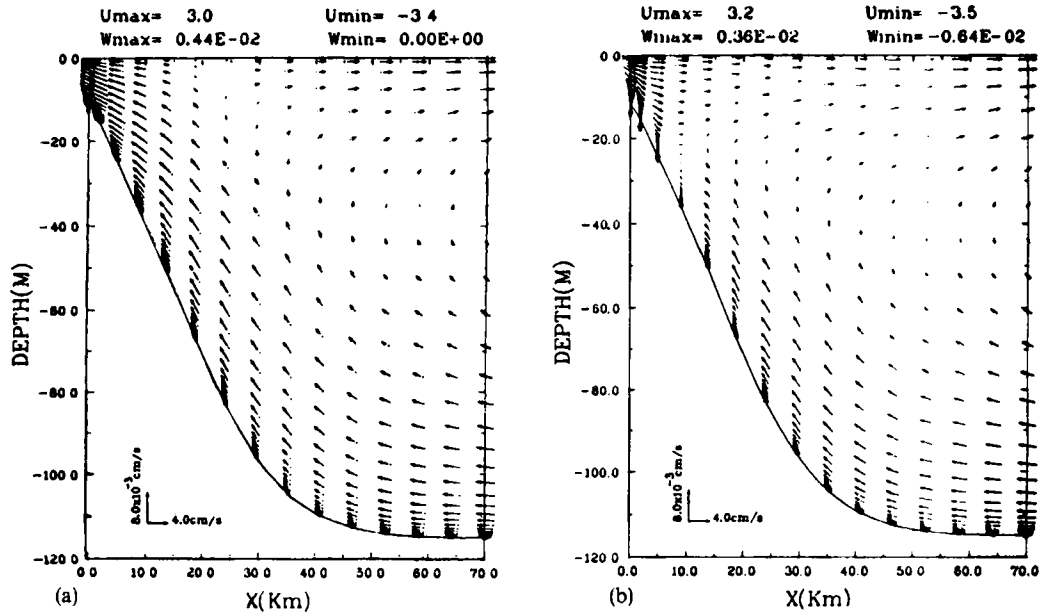

Figure 6. Computed velocity vectors at day 2 in a vertical cross-shelf plane off $j=9$: (a) without river discharge; (b) with river discharge

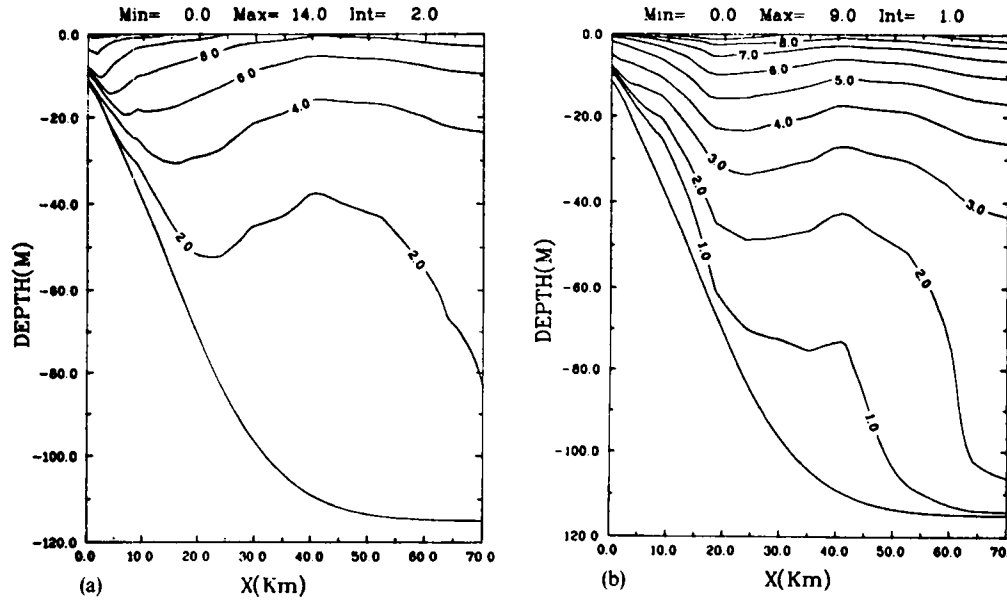

Figure 7. Isolines of the computed longshore currents (cm s^{-1}) at day 2 in a vertical cross-shelf plane off $j=9$: (a) without river discharge; (b) with river discharge

7(a) that when there is no river discharge, an intense core of longshore current is seen in the near-surface region adjacent to the coastline with a maximum speed of about 14 cm s^{-1}. In the case when the river discharge is included [Figure 7(b)], the maximum speed of the current is reduced to 9 cm s^{-1}.

Figure 8 shows a comparison of the thermal field in a horizontal plane at day 6 in the region subject to south-westerly wind stress forcing, with and without considering the river discharge. Figure 8(a) shows that when the discharge is absent, the surface temperature near the coast has further reduced to 29·2°C. There is an increase in the sea-surface temperature in the northern part of the forced zone, which is caused due to the strong non-linear effect, as discussed earlier in Figure 3(a).

When the river discharge is taken into account [Figure 8(b)], a reduction of coastal upwelling is apparent, which is indicated by the replacement of the isotherm corresponding to a temperature of 29·2°C near the coast by that of 29·6°C.

Examination of Figures 3(a) and (b) and 8(a) and (b) reveals that the effect of the river discharge on surface temperature is more to the north of the location of the Godavari River than to the south.

Figure 9 provides a comparison of the vertical thermal structure at day 6 in a cross-shelf vertical plane off $j=9$, with and without the inclusion of the river discharge. It may be seen from Figure 9(a) that when there is no river discharge, the temperature of the near-coastal core of surface water has reduced further to 29·2°C. Farther off-shore, the isotherm corresponding to a temperature of 29·5°C outcrops at the ocean surface. In the case when the discharge is included [Figure 9(b)], the coastal upwelling is further reduced, which is evident from the downward tilting of one more isotherm corresponding to a temperature of 29·5°C.

Figure 10 gives a comparison of a plan view of computed surface current vectors at day 6 in the region subject to south-westerly wind stress forcing, with and without the effect of river discharge.

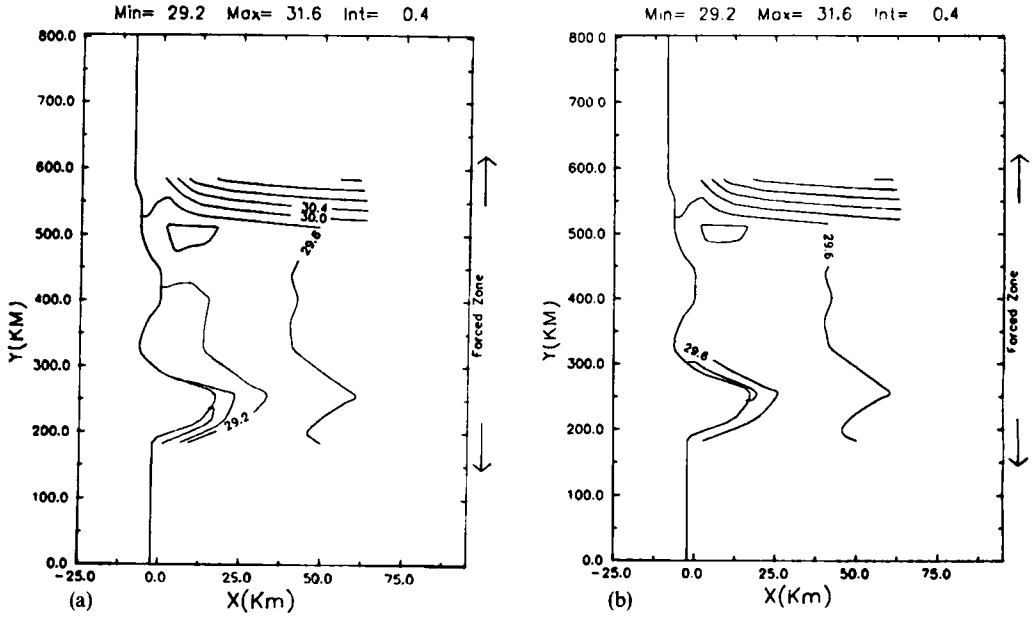

Figure 8. The computed thermal field (°C) in a horizontal plane at day 6: (a) without river discharge; (b) with river discharge

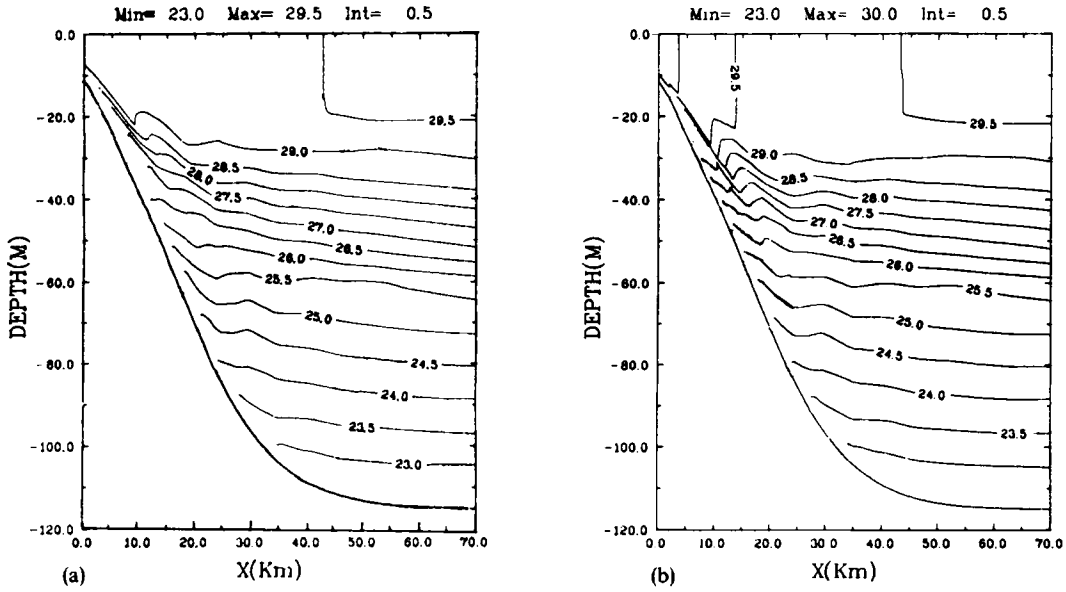

Figure 9. The computed thermal field (°C) off $j=9$ at day 6: (a) without river discharge; (b) with river discharge

It may be seen from Figure 10(a) that when the discharge is absent, the surface currents are aligned in an easterly direction, away from the coast. In the immediate vicinity of the coastline, the currents are constrained to flow along the coast. Maximum off-shore cross-shelf velocities are about 4 cm s^{-1}, while the on-shore velocities induced locally by the curving coastline near Kakinada have maxima of about 2 cm s^{-1}. Maximum longshore velocities are about 18 cm s^{-1}.

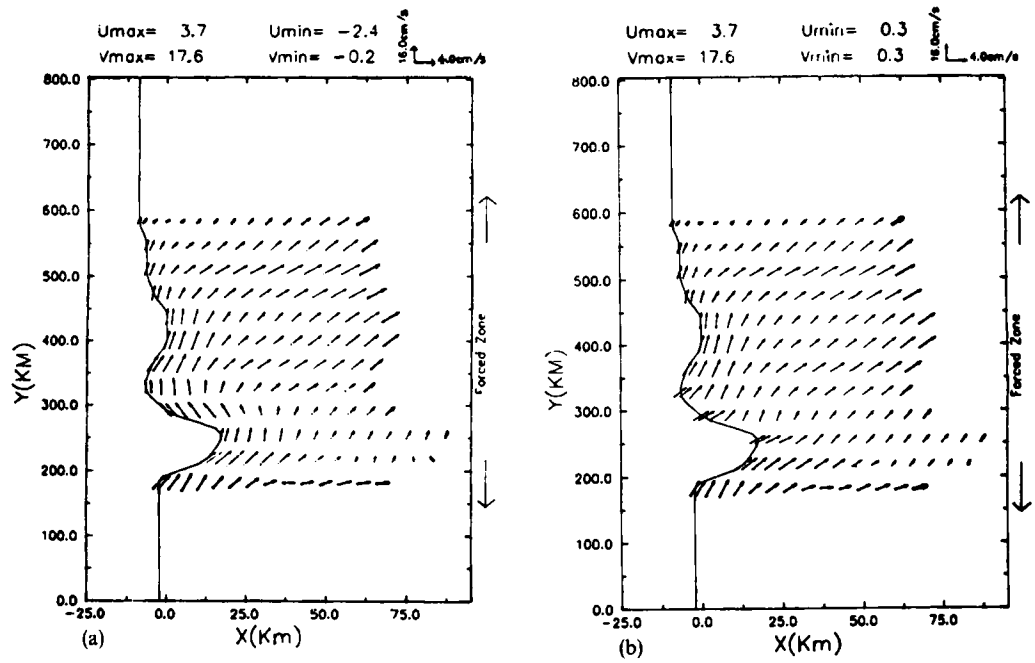

Figure 10. Plan view of the computed surface current vectors at day 6: (a) without river discharge; (b) with river discharge

When the river discharge is taken into account [Figure 10(b)], the surface currents in the zone within about 25 km off the coastline and 250–325 km in the alongshore direction change and flow eastwards.

Figure 11 shows a comparison of vertical current structure at day 6 in a cross-shelf vertical plane off $j=9$, with and without the inclusion of the river discharge. It may be seen from Figure 11(a) that when there is no river discharge, an off-shore surface flow is apparent with a maximum speed of about 1·5 cm s^{-1}, with the exception of a strong on-shore surface flow with a maximum velocity of about 2·8 cm s^{-1} within about 27 km of the coastline. This strong on-shore surface flow is the part of western boundary current flowing along the coast as shown in Figure 10(a).

When the river discharge is included [Figure 11(b)], the strong on-shore flow near the coast is replaced by an off-shore one, leading to a maximum current velocity of about 3 cm s^{-1} near the coast.

Figure 11(a) depicts the existence of strong upwelling in this cross-section with a maximum speed of about $3{\cdot}5\times10^{-3}$ cm s^{-1}, while in case of Figure 11(b), it has reduced to $2{\cdot}6\times10^{-3}$ cm s^{-1}. Figure 11(b) also shows the existence of strong downwelling with a maximum speed of about $6{\cdot}8\times10^{-3}$ cm s^{-1}.

Figure 12 provides a comparison of the isolines of vertical longshore velocity structure at day 6 in a cross-shelf vertical plane off $j=9$, with and without considering the effect of river discharge. It may be seen from Figure 12(a) that when the river discharge is absent, there is an intense core of longshore current in the near-surface region adjacent to the coastline. It has a maximum speed of about 14 cm s^{-1} and a width of about 29 km from the coastline. However, at a depth of about 100 m and at a distance from the coastline of about 40 km, there is a predicted weak current flowing in the direction opposite to that of the surface current. Maximum velocity in this

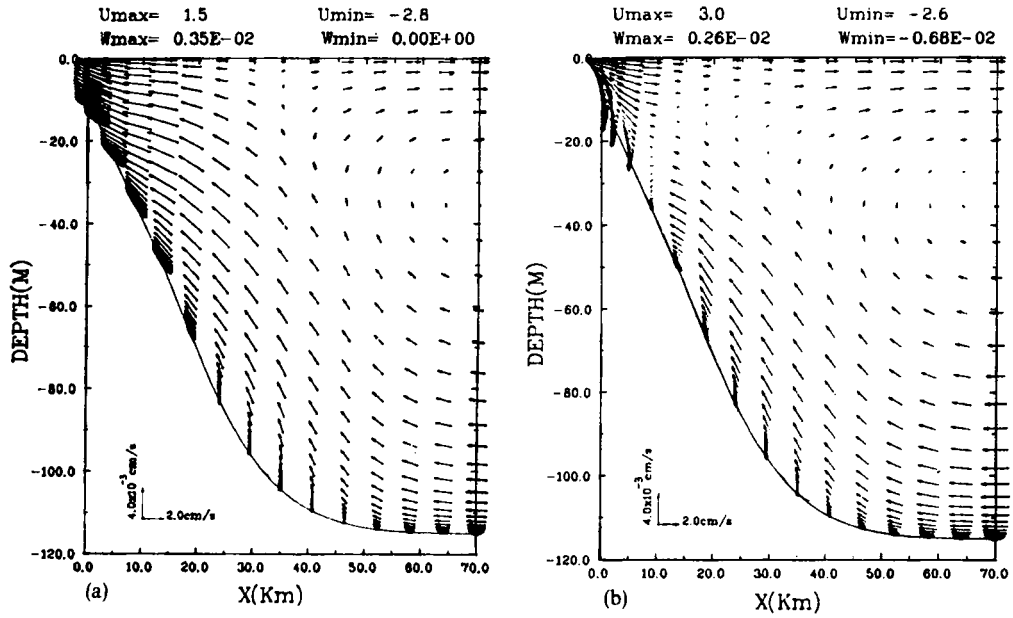

Figure 11. Computed velocity vectors at day 6 in a vertical cross-shelf plane off $j=9$: (a) without river discharge; (b) with river discharge

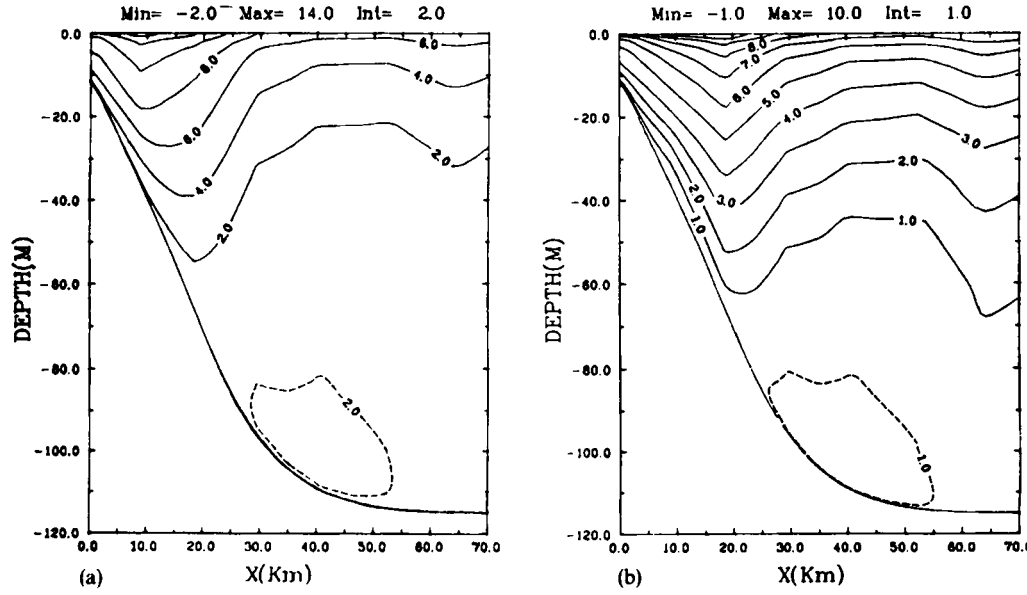

Figure 12. Isolines of the computed longshore current (cm s^{-1}) at day 6 in a vertical cross-shelf plane off $j=9$: (a) without river discharge; (b) with river discharge

countercurrent is about $2\,cm\,s^{-1}$. In the case when the river discharge is considered [Figure 12(b)], the speed of the longshore current is reduced to $10\,cm\,s^{-1}$ and the width is increased to 35 km from the coastline in comparison to that of 29 km in Figure 12(a). In addition, there is also a reduction of the speed of the countercurrent to $1\,cm\,s^{-1}$ [Figure 12(b)]. These figures demonstrate that mass balance does not take place only in a two-dimensional plane alone, such as in a vertical or a horizontal plane; in fact, mass balance takes place three-dimensionally.

CONCLUSIONS

A three-dimensional continuously stratified coastal ocean circulation model was applied to study the effect of river discharge on the coastal circulation in the western Bay of Bengal. An open boundary was put at the location of the Godavari River on the east coast of India. Numerical experiments were performed by prescribing the river discharge. The computed results have shown that the incorporation of the discharge suppresses the upwelling near the river mouth and the effect of the river discharge on the surface temperature is more to the north of the location of the Godavari River than to the south. Unfortunately, there is no observational data to use in a validation procedure.

REFERENCES

1. B. Johns, G. S. Rao, S. K. Dube and P. C. Sinha, 'An application of a wind-driven coastal upwelling model in the western Bay of Bengal', *Continental Shelf Res.*, **11**, 295–319 (1991).
2. L. V. G. Rao and R. Jayaraman, 'Hydrodynamical features of the southern and central Bay of Bengal during the transition period between winter and summer', *Bull. Natl. Inst. Sci. India*, **38**, 184–205 (1968).
3. D. P. Rao, 'A comparative study of some physical processes governing the potential productivity of the Bay of Bengal and Arabian Sea', Ph.D. Thesis, Andhra Univ., Waltaire, 1977.
4. V. V. Gopal Krishna and J. S. Sastry, 'Surface circulation over the shelf off the east coast of India during the south-west monsoon', *Ind. J. Mar. Sci.*, **14**, 62–65 (1985).
5. B. Johns, P. C. Sinha, S. K. Dube, U. C. Mohanty and A. D. Rao, 'Simulation of storm surges using a three-dimensional numerical model: an Application to the 1977 Andhra Cyclone', *Q. J. R. Meteor. Soc.*, **109**, 211–224 (1983).
6. B. Johns, 'The modelling of tidal flow in a channel using a turbulence energy closure scheme', *J. Phys. Oceanogr.*, **8**, 1042–1049 (1978).
7. P. J. Roache, *Computational Fluid Dynamics*, Hermoza Publishers, 1972, p. 434.
8. B. Johns, A. D. Rao, S. K. Dube and P. C. Sinha, 'Numerical modelling of tide-surge interaction in the Bay of Bengal', *Phil. Trans. Roy. Soc. A* **313**, 507–535 (1985).
9. T. V. N. Rao, D. P. Rao, B. P. Rao and V. S. R. Raju, 'Upwelling and sinking along the Vishakhapatnam Coast', *Ind. J. Mar. Sci.*, **15**, 84–87 (1986).